REMUNOM
ISSN 2178-6925

Received: 19/09/2026 - **Accepted:** 18/10/2026
Vol: 13.22
DOI: 10.66104/t71wyw54
Pages: 1-34

LOCAL DISORDER WITHIN LONG-RANGE ORDER: EVIDENCE FROM Eu^{3+} LUMINESCENCE AND RAMAN SPECTROSCOPY IN $La_2Zr_2O_7$ PYROCHLORE CERAMICS

DESORDEM LOCAL NA ORDEM DE LONGO ALCANCE: INDÍCIOS PELA LUMINESCÊNCIA DO Eu^{3+} E PELA ESPECTROSCOPIA RAMAN EM CERÂMICAS PIROCLORO DE $La_2Zr_2O_7$

DESORDEN LOCAL DENTRO DEL ORDEN DE LARGO ALCANCE: INDICIOS A PARTIR DE LA LUMINISCENCIA DEL Eu^{3+} Y DE LA ESPECTROSCOPIA RAMAN EN CERÁMICAS PIROCLORO DE $La_2Zr_2O_7$

João Dionízio de Melo Neto

Doutorando, Laboratório de Filmes Finos em Energias Renováveis (LAFFER), Programa de Pós-Graduação em Engenharia e Ciência de Materiais (PGMateriais), da Universidade Federal do Ceará (UFC), Fortaleza, CE, Brasil

E-mail: joao.dionizio@ifce.edu.br

Orcid: 0000-0003-1054-0257

Felipe Rodrigues da Silva

Doutorando, Laboratório de Filmes Finos em Energias Renováveis (LAFFER), Programa de Pós-Graduação em Engenharia e Ciência de Materiais (PGMateriais), da Universidade Federal do Ceará (UFC), Fortaleza, CE, Brasil

E-mail: prof.feliperodrigues18@gmail.com

Orcid: 0000-0003-1224-8364

Yuri Gomes dos Santos

Doutorando, Programa de Pós-Graduação em Física (PPGFis), Departamento de Física, da Universidade Federal do Ceará (UFC), Fortaleza, CE, Brasil

E-mail: yuri@fisica.ufc.br

Orcid: 0009-0000-3413-5964

CC BY

REMUNOM
ISSN 2178-6925

Received: 19/09/2026 - **Accepted:** 18/10/2026
Vol: 13.22
DOI: 10.66104/t71wyw54
Pages: 1-34

José Souto Sarmento

Doutor, Grupo de Química de Materiais Avançados (GQMat), Departamento de Química Analítica e Físico-Química, Universidade Federal do Ceará (UFC), Fortaleza, CE, Brasil

E-mail: josesoutosarmento@gmail.com

Orcid: 0009-0003-1161-4999

William Neves da Silva

Doutorando, Departamento de Engenharia de Produção, Universidade Federal de Santa Catarina, Florianópolis, SC, Brasil

E-mail: williamrns88@gmail.com

Orcid: 0000-0002-4731-095X

João Paulo Costa do Nascimento

Doutor, Laboratório de Telecomunicações e Ciência e Engenharia de Materiais (LOCEM), Departamento de Física, da Universidade Federal do Ceará (UFC), Fortaleza, CE, Brasil

E-mail: jpquimico3@gmail.com

Orcid: 0000-0002-6236-7284

Antonio Jefferson Mangueira Sales

Doutor, Laboratório de Telecomunicações e Ciência e Engenharia de Materiais (LOCEM), Núcleo de Tecnologia e Qualidade Industrial do Ceará - Nutec, Campus do Pici, Universidade Federal do Ceará (UFC), Fortaleza, CE, Brasil

E-mail: jeffsales.brasil@gmail.com

Orcid: 0000-0002-1970-0547

Mairton Cavalcante Romeu

Doutor, Professor titular do Departamento de Física e Matemática, campus Fortaleza, Instituto Federal do Ceará (IFCE), Fortaleza, CE, Brasil

E-mail: mairtoncavalcante@ifce.edu.br

CC BY

REMUNOM
ISSN 2178-6925

Received: 19/09/2026 - **Accepted:** 18/10/2026
Vol: 13.22
DOI: 10.66104/t71wyw54
Pages: 1-34

Orcid: 0000-0001-5204-9031

Francisco Nivaldo Aguiar Freire

Doutor, Laboratório de Filmes Finos em Energias Renováveis (LAFFER),

Professor Titular do Departamento de Engenharia Metalúrgica e de Materiais,

Universidade Federal do Ceará (UFC), Fortaleza, CE, Brasil

E-mail: nivaldo@ufc.br

Orcid: 0000-0001-5449-2635

Abstract

$La_2Zr_2O_7$ (LZO) pyrochlore is a thermally and chemically stable host for luminescent lanthanide ions, but most studies on Eu^{3+}-doped LZO concern nanoparticles prepared by chemical routes. In this work, undoped LZO and LZO doped with 1, 2 and 4 mol% Eu^{3+} were synthesized by solid-state reaction at 1200 °C and characterized by X-ray diffraction with Rietveld refinement, Raman spectroscopy, scanning electron microscopy, UV-Vis diffuse reflectance and photoluminescence. X-ray diffraction showed the ordered cubic pyrochlore as the main phase, with superstructure reflections and no lattice-parameter trend resolvable within the experimental uncertainty, consistent with the substitutional incorporation of Eu^{3+} on the La^{3+} site. Raman spectra confirmed the pyrochlore vibrational modes and revealed a small amount of residual monoclinic ZrO_2 in all samples. Particles with mean Feret diameters of 298–324 nm were slightly larger in the doped samples, regardless of the Eu^{3+} content, with no change in shape, a difference observed in a single synthesis batch per composition. The host showed an absorption onset of 4.61 eV, estimated by the Tauc method for a direct transition, and doping introduced the $O^{2-}\rightarrow Eu^{3+}$ charge-transfer band at 255–258 nm, which lowers the apparent onset to 4.50 eV. Under 355 nm excitation, the $^5D_0\rightarrow{}^7F_J$ emission of Eu^{3+} increased with dopant content, and no decrease in the integrated emission was observed up to 4 mol% under the experimental conditions used. The asymmetry ratio (1.33–1.89) lay between the value expected for the centrosymmetric pyrochlore site and those reported for nanoparticles. Its increase at 4 mol%, together with the broadening of the 299 cm^{-1} Raman band quantified by Voigt profile fitting (FWHM from 14.5 ± 0.2 to 16.5 ± 0.2 cm^{-1}), provides evidence compatible with increased local disorder around the optically excited Eu^{3+} centers at this content, while the long-range pyrochlore order is preserved.
Keywords: Lanthanum zirconate; Pyrochlore; Europium; Photoluminescence; Raman spectroscopy.

Resumo

O pirocloro $La_2Zr_2O_7$ (LZO) é uma matriz térmica e quimicamente estável para íons lantanídeos luminescentes, mas a maior parte dos estudos sobre o LZO dopado com Eu^{3+} trata de nanopartículas obtidas por rotas químicas. Neste trabalho, o LZO puro e dopado com 1, 2 e 4 mol% de Eu^{3+} foi sintetizado por reação no estado sólido a 1200 °C e caracterizado por difração de raios X com refinamento de Rietveld, espectroscopia Raman, microscopia eletrônica de varredura, reflectância difusa no UV-Vis e fotoluminescência. A difração de raios X mostrou o pirocloro cúbico ordenado como fase majoritária, com reflexões de superestrutura e sem tendência do parâmetro de rede resolvível dentro da incerteza experimental, o que é compatível com a incorporação substitucional do Eu^{3+} no sítio do La^{3+}. Os espectros Raman confirmaram os modos vibracionais do pirocloro e revelaram uma pequena quantidade de ZrO_2 monoclínico residual em todas as amostras. As partículas, com diâmetro de Feret médio entre 298 e 324 nm, foram ligeiramente maiores nas amostras dopadas, independentemente do teor de Eu^{3+}, sem alteração de forma, diferença observada em uma única síntese por composição. A matriz apresentou limiar de absorção de 4,61

CC BY

REMUNOM
ISSN 2178-6925

Received: 19/09/2026 - **Accepted:** 18/10/2026
Vol: 13.22
DOI: 10.66104/t71wyw54
Pages: 1-34

eV, estimado pelo método de Tauc para transição direta, e a dopagem introduziu a banda de transferência de carga $O^{2-}\rightarrow Eu^{3+}$ entre 255 e 258 nm, que reduz o limiar aparente para 4,50 eV. Sob excitação em 355 nm, a emissão $^5D_0\rightarrow{}^7F_J$ do Eu^{3+} aumentou com o teor de dopante, e não se observou diminuição da emissão integrada até 4 mol% nas condições experimentais empregadas. A razão de assimetria (1,33–1,89) situou-se entre o valor esperado para o sítio centrossimétrico do pirocloro e os relatados para nanopartículas. Seu aumento em 4 mol%, junto com o alargamento da banda Raman em 299 cm^{-1} quantificado por ajuste de perfil Voigt (FWHM de 14,5 ± 0,2 para 16,5 ± 0,2 cm^{-1}), constitui evidência compatível com aumento da desordem local em torno dos centros de Eu^{3+} opticamente excitados nesse teor, com preservação da ordem pirocloro de longo alcance.
Palavras-chave: Zirconato de lantânio; Pirocloro; Európio; Fotoluminescência; Espectroscopia Raman.

Resumen

El pirocloro $La_2Zr_2O_7$ (LZO) es una matriz térmica y químicamente estable para iones lantánidos luminiscentes, pero la mayoría de los estudios sobre el LZO dopado con Eu^{3+} tratan de nanopartículas obtenidas por rutas químicas. En este trabajo, el LZO puro y dopado con 1, 2 y 4 mol% de Eu^{3+} se sintetizó por reacción en estado sólido a 1200 °C y se caracterizó mediante difracción de rayos X con refinamiento de Rietveld, espectroscopia Raman, microscopía electrónica de barrido, reflectancia difusa UV-Vis y fotoluminiscencia. La difracción de rayos X mostró el pirocloro cúbico ordenado como fase mayoritaria, con reflexiones de superestructura y sin una tendencia del parámetro de red resoluble dentro de la incertidumbre experimental, lo que es compatible con la incorporación sustitucional del Eu^{3+} en el sitio del La^{3+}. Los espectros Raman confirmaron los modos vibracionales del pirocloro y revelaron una pequeña cantidad de ZrO_2 monoclínico residual en todas las muestras. Las partículas, con diámetro de Feret medio entre 298 y 324 nm, fueron ligeramente mayores en las muestras dopadas, independientemente del contenido de Eu^{3+}, sin cambios de forma, diferencia observada en una única síntesis por composición. La matriz presentó un umbral de absorción de 4,61 eV, estimado por el método de Tauc para transición directa, y el dopaje introdujo la banda de transferencia de carga $O^{2-}\rightarrow Eu^{3+}$ entre 255 y 258 nm, que reduce el umbral aparente a 4,50 eV. Bajo excitación a 355 nm, la emisión $^5D_0\rightarrow{}^7F_J$ del Eu^{3+} aumentó con el contenido de dopante, y no se observó disminución de la emisión integrada hasta 4 mol% en las condiciones experimentales empleadas. La razón de asimetría (1,33–1,89) se situó entre el valor esperado para el sitio centrosimétrico del pirocloro y los reportados para nanopartículas. Su aumento con 4 mol%, junto con el ensanchamiento de la banda Raman en 299 cm^{-1} cuantificado mediante ajuste de perfil Voigt (FWHM de 14,5 ± 0,2 a 16,5 ± 0,2 cm^{-1}), constituye evidencia compatible con un aumento del desorden local en torno a los centros de Eu^{3+} ópticamente excitados en ese contenido, con preservación del orden pirocloro de largo alcance.
Palabras clave: Circonato de lantano; Pirocloro; Europio; Fotoluminiscencia; Espectroscopia Raman.

1. Introduction

Oxides with the pyrochlore-type structure, of general formula $A_2B_2O_7$, form a broad family of ceramic materials in which the A site is usually occupied by a trivalent rare-earth cation and the B site by a tetravalent cation (PANGHAL et al., 2019; SUBRAMANIAN; ARAVAMUDAN; SUBBA RAO, 1983). The cubic pyrochlore structure (space group *Fd*$\bar{3}$*m*) can be described as a derivative of the fluorite structure (*Fm*$\bar{3}$*m*), in which the cations order on distinct crystallographic sites and one in every eight oxygen anions is removed in an ordered manner

CC BY

REMUNOM
ISSN 2178-6925

Received: 19/09/2026 - **Accepted:** 18/10/2026
Vol: 13.22
DOI: 10.66104/t71wyw54
Pages: 1-34

(HOLLIDAY et al., 2013; SUBRAMANIAN; ARAVAMUDAN; SUBBA RAO, 1983). When this ordering is lost and cations and oxygen vacancies become randomly distributed, the defect fluorite is obtained, in which the cation site is poorly defined because of the random distribution of oxygen vacancies (HOLLIDAY et al., 2013). The stability of the ordered pyrochlore depends mainly on the cation ionic radius ratio, r_A/r_B, which should lie approximately between 1.46 and 1.78 (PANGHAL et al., 2019; SUBRAMANIAN; ARAVAMUDAN; SUBBA RAO, 1983), and also on the heat-treatment temperature and time, which favor cation and anion ordering (PANGHAL et al., 2019). This structural versatility, combined with high thermal and chemical stability, explains the interest in these compounds for applications such as radioactive waste immobilization, oxidation catalysis, oxygen sensors and thermal barrier coatings (PANGHAL et al., 2019; ZHU et al., 2018).

Among the rare-earth zirconates, lanthanum zirconate, $La_2Zr_2O_7$ (LZO), stands out for combining low thermal conductivity, a high melting point and excellent phase stability (PANGHAL et al., 2019). Because La^{3+} is a cation with a large ionic radius, LZO has an r_A/r_B ratio of about 1.61, calculated with the Shannon (1976) ionic radii for La^{3+} (coordination number 8) and Zr^{4+} (coordination number 6), well above the lower stability limit of the pyrochlore (POKHREL et al., 2017). By solid-state reaction between La_2O_3 and ZrO_2, single-phase pyrochlore, with the (111) superstructure reflection characteristic of cation ordering, is already obtained at 1200 °C, with a lattice parameter close to 10.80 Å, and the degree of cation–anion order increases with heat-treatment temperature and time (PANGHAL et al., 2019). From an electronic standpoint, first-principles calculations describe LZO as a wide-gap insulator whose valence band is formed mainly by O 2*p* states and whose conduction band is formed by La 5*d* and Zr 4*d* states, so that the absorption edge corresponds to a charge transfer from oxygen to the cations (YANG et al., 2016). The calculated band gap is direct, at the Γ point, with values between 4.01 and 4.40 eV depending on the functional used (ABBAS et al., 2022; IQBAL et al., 2025; YANG et al., 2016). The width of this band gap and the existence of a cation site suitable for substitution by trivalent lanthanide ions make LZO an attractive host

CC BY

REMUNOM
ISSN 2178-6925

Received: 19/09/2026 - **Accepted:** 18/10/2026
Vol: 13.22
DOI: 10.66104/t71wyw54
Pages: 1-34

for luminescent materials, including scintillators, in which the high atomic numbers of La and Zr favor X-ray attenuation (POKHREL; ALCOUTLABI; MAO, 2017).

The Eu^{3+} ion is one of the most studied activators, both for its intense red emission at about 612 nm and for its usefulness as a structural probe (BINNEMANS, 2015; POKHREL; ALCOUTLABI; MAO, 2017). Because the $^7F_0$ ground state and the $^5D_0$ emitting state are non-degenerate, the $^5D_0 \rightarrow {}^7F_J$ transitions directly reflect the symmetry and homogeneity of the environment around the ion (BINNEMANS, 2015). The magnetic-dipole $^5D_0 \rightarrow {}^7F_1$ transition is little influenced by the environment, whereas the electric-dipole $^5D_0 \rightarrow {}^7F_2$ transition is hypersensitive and is forbidden when the ion occupies a site with an inversion center (BINNEMANS, 2015). For this reason, the asymmetry ratio, $R = I(^5D_0 \rightarrow {}^7F_2)/I(^5D_0 \rightarrow {}^7F_1)$, is widely used to assess the local distortion around Eu^{3+} (BINNEMANS, 2015). In LZO, Eu^{3+} replaces La^{3+}, which has the same charge and a similar ionic radius, rather than the much smaller Zr^{4+} (ALAPARTHI et al., 2014). In the ordered pyrochlore, this site has D_{3d} symmetry, with an inversion center, so that the magnetic-dipole transition should predominate: Holliday et al. (2013) observed, for Eu^{3+} in a pyrochlore environment, a predominance of the $^5D_0 \rightarrow {}^7F_1$ transition, with $R \approx 0.4$, whereas in the defect fluorite environment the ratio is reversed ($R \approx 2.5$), and showed that Eu^{3+} luminescence detects local disorder with greater sensitivity than X-ray diffraction. In addition to the *f–f* transitions, Eu^{3+} in oxides shows a broad excitation band in the ultraviolet, assigned to $O^{2-} \rightarrow Eu^{3+}$ charge transfer, located at about 255–258 nm in LZO (MOHAPATRA et al., 2015; POKHREL; ALCOUTLABI; MAO, 2017). This band overlaps the absorption edge of the host and is the most efficient excitation pathway for the red emission of Eu^{3+} in this system (POKHREL; ALCOUTLABI; MAO, 2017).

Despite this potential, the literature on $La_2Zr_2O_7:Eu^{3+}$ focuses on nanoparticles prepared by chemical routes, such as molten-salt synthesis (ALAPARTHI et al., 2014; POKHREL; ALCOUTLABI; MAO, 2017), gel combustion (MOHAPATRA et al., 2015) and coprecipitation followed by core@shell coating (POKHREL et al., 2017), with emphasis on emission intensity, quantum yield and scintillation. In these nanosized materials, the structure often appears as fluorite in

CC BY

REMUNOM
ISSN 2178-6925

Received: 19/09/2026 - **Accepted:** 18/10/2026
Vol: 13.22
DOI: 10.66104/t71wyw54
Pages: 1-34

the diffraction patterns, without the pyrochlore superstructure reflections (ALAPARTHI et al., 2014; POKHREL; ALCOUTLABI; MAO, 2017; POKHREL et al., 2017), and surface defects and oxygen vacancies affect the luminescence (GUPTA et al., 2019; POKHREL et al., 2017). The results also diverge regarding the optimum Eu^{3+} concentration: about 4 mol% in samples prepared by gel combustion (MOHAPATRA et al., 2015), and from 15 mol% (POKHREL; ALCOUTLABI; MAO, 2017) and 32.5 mol% (ALAPARTHI et al., 2014) in nanoparticles prepared in molten salts, which indicates a strong dependence on the synthesis route and microstructure. Solid-state reaction, the classical route for preparing pyrochlores (SUBRAMANIAN; ARAVAMUDAN; SUBBA RAO, 1983) and the one used for LZO by Panghal et al. (2019), has been little explored for the Eu^{3+}-doped system, and studies on dense LZO:Eu^{3+} ceramics have focused mainly on thermophysical properties for thermal barriers (ZHU et al., 2018). Holliday et al. (2013), in turn, have already shown that Eu^{3+} luminescence distinguishes pyrochlore and defect fluorite environments in LZO; the present work does not aim to establish this principle, but to apply it, together with Raman spectroscopy, to ceramics obtained by solid-state reaction in the dilute regime, in which long-range order is established and the interest lies in the local disorder introduced by the dopant. Moreover, in the studies consulted, the influence of Eu^{3+} on the absorption edge of the host has not been determined experimentally by diffuse reflectance. Thus, in the literature consulted, no study was found that combines, for LZO:Eu^{3+} samples obtained by solid-state reaction with low dopant contents, structural refinement by the Rietveld method, Raman spectroscopy, band-gap energy determination and photoluminescence analysis.

In this context, the present work aims to synthesize undoped $La_2Zr_2O_7$ and $La_2Zr_2O_7$ doped with 1, 2 and 4 mol% Eu^{3+} ($La_{2-x}Eu_xZr_2O_7$, with x = 0, 0.02, 0.04 and 0.08) by solid-state reaction and to correlate the crystal structure, determined by X-ray diffraction and Rietveld refinement, the local order, assessed by Raman spectroscopy, the morphology, observed by scanning electron microscopy, and the optical properties, assessed by UV-Vis diffuse reflectance spectroscopy and photoluminescence. The 1–4 mol% contents were chosen because they lie in the

CC BY

REMUNOM
ISSN 2178-6925

Received: 19/09/2026 - **Accepted:** 18/10/2026
Vol: 13.22
DOI: 10.66104/t71wyw54
Pages: 1-34

dilute regime, up to the optimum concentration reported for samples prepared by gel combustion (MOHAPATRA et al., 2015) and below the contents at which concentration quenching was observed in nanoparticles (ALAPARTHI et al., 2014; POKHREL; ALCOUTLABI; MAO, 2017), which allows the initial effects of Eu^{3+} incorporation to be assessed without interference from this phenomenon. In particular, the aim is to examine how low Eu^{3+} contents affect the lattice parameter, the absorption edge and the charge-transfer band of the host, as well as the local environment of the dopant, assessed by the asymmetry ratio *R* and compared with the local disorder indicated by the Raman spectrum. Beyond its fundamental interest, understanding local disorder in LZO:Eu^{3+} is relevant to its use as a red phosphor and as a ceramic host for radioactive waste immobilization, in which Eu^{3+} is used as a non-radioactive analogue of trivalent actinides (HOLLIDAY et al., 2013).

2. Materials and Methods

2.1. Sample synthesis

Undoped and Eu^{3+}-doped $La_2Zr_2O_7$ (LZO) samples were prepared by the solid-state reaction method. The starting reagents were the oxides La_2O_3 (Vetec, 99.99%), ZrO_2 (Sigma-Aldrich, 99.99%) and Eu_2O_3 (Sigma-Aldrich, 99.99%), used as received.

Doping was designed considering the partial substitution of La^{3+} ions by Eu^{3+} ions on the A site of the pyrochlore structure, according to the nominal composition $La_{2-x}Eu_xZr_2O_7$, with x = 0, 0.02, 0.04 and 0.08. These values correspond to 0, 1, 2 and 4 mol% Eu^{3+} relative to the total A-site cations (La^{3+} + Eu^{3+}), and the samples were labeled LZO, LZO:Eu1%, LZO:Eu2% and LZO:Eu4%, respectively. The reagent masses were calculated from the stoichiometric relations of each composition to obtain 10 g of product, as shown in Table 1.

Table 1. Nominal composition and reagent masses used in the synthesis of 10 g of each sample.

Sample	Nominal composition	La_2O_3 (g)	ZrO_2 (g)	Eu_2O_3 (g)

CC BY

REMUNOM
ISSN 2178-6925

Received: 19/09/2026 - **Accepted:** 18/10/2026
Vol: 13.22
DOI: 10.66104/t71wyw54
Pages: 1-34

LZO	$La_2Zr_2O_7$	5.6934	4.3066	–
LZO:Eu1%	$La_{1.98}Eu_{0.02}Zr_2O_7$	5.6339	4.3046	0.0615
LZO:Eu2%	$La_{1.96}Eu_{0.04}Zr_2O_7$	5.5745	4.3026	0.1229
LZO:Eu4%	$La_{1.92}Eu_{0.08}Zr_2O_7$	5.4557	4.2987	0.2455

Source: Prepared by the authors (2026).

As shown in Table 1, the increase in Eu_2O_3 content was accompanied by a proportional reduction in the La_2O_3 mass, keeping constant the molar ratio between the A-site (La^{3+} + Eu^{3+}) and B-site (Zr^{4+}) cations, equal to 1:1. Thus, the structural and optical differences observed between the samples can be attributed to the dopant concentration rather than to differences in nominal stoichiometry between the compositions. Because La_2O_3 was used without prior drying, the effective stoichiometry may show a small lanthanum deficiency, common to all samples (Section 3.2).

The oxides were homogenized in a planetary ball mill (Fritsch, Pulverisette 5) at 360 rpm for 6 h, in polyacetal jars containing 97.8 g of zirconia (ZrO_2) balls and 10 g of the powder mixture, under dry conditions. The purpose of milling was to homogenize the mixture and reduce the particle size of the reagents, increasing the contact area between them and favoring the diffusion processes that govern the solid-state reaction.

The powders were then transferred to alumina crucibles and calcined in a resistive furnace (Jung, LF 00916) at 1200 °C for 4 h, with heating and cooling rates of 5 °C min^{-1}. The doped samples were subjected to the same milling and calcination conditions used for the undoped host, to ensure comparability between the compositions. The synthesis procedure is outlined in Figure 1.

CC BY

REMUNOM
ISSN 2178-6925

Received: 19/09/2026 - **Accepted:** 18/10/2026
Vol: 13.22
DOI: 10.66104/t71wyw54
Pages: 1-34

Figure 1. Scheme of the solid-state synthesis of the samples: mixing of the precursor oxides, milling in a planetary ball mill (360 rpm, 6 h), calcination at 1200 °C for 4 h, and the resulting $La_2Zr_2O_7$ powders with 0, 1, 2 and 4 mol% Eu^{3+}.

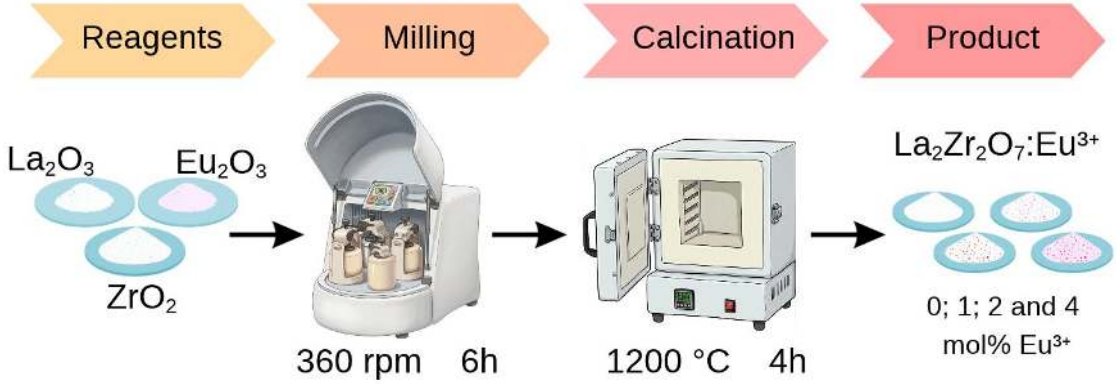

Source: Prepared by the authors (2026).

2.2. X-ray diffraction and Rietveld refinement

The crystal structure of the samples was investigated by X-ray diffraction (XRD) on a PANalytical X'Pert PRO MPD diffractometer, with Co Kα radiation (λ = 1.78896 Å), operating at 40 kV and 40 mA. The patterns were collected over the 2θ range of 10° to 100°, with a step of 0.013°, in parallel-beam geometry with a monochromator, a 1/4° divergence slit, 0.02 rad Soller slits and a spinning sample holder (*spinner*).

Structural refinement was performed by the Rietveld method using the GSAS-II *software* (RIETVELD, 1969; TOBY; VON DREELE, 2013). The cubic pyrochlore structure of $La_2Zr_2O_7$, space group $Fd\bar{3}m$ (No. 227), described in crystallographic card ICSD No. 15165 (DEISEROTH; MÜLLER-BUSCHBAUM, 1970), was adopted as the starting model. For LZO and LZO:Eu4%, whose m-ZrO_2 reflections were not resolved, pyrochlore was considered the only phase. For the LZO:Eu1% and LZO:Eu2% samples, measured on a glass support coated with fluorine-doped tin oxide (FTO), monoclinic zirconia (baddeleyite, $P2_1/c$; ICSD No. 41010; KUDOH; TAKEDA; ARASHI, 1986) was included as a secondary phase, and the (200) reflection of SnO_2 from the substrate, at about 44.3° (2θ), was not included in the model. The scale factor, background, peak-profile and lattice parameters were refined. The quality of the fit was assessed by the *wR* (weighted

CC BY

REMUNOM
ISSN 2178-6925

Received: 19/09/2026 - **Accepted:** 18/10/2026
Vol: 13.22
DOI: 10.66104/t71wyw54
Pages: 1-34

profile), GOF (goodness of fit) and reduced χ^2 indices. In GSAS-II, the GOF corresponds to the square root of the reduced χ^2. The statistical uncertainties (esd) of the lattice parameters were estimated from the refined profiles; because the lattice parameter is correlated with the sample displacement relative to the focal plane, the systematic uncertainty, of the order of 0.01 Å, is much larger than the esd and was considered in the comparison between samples (Section 3.1).

2.3. Raman spectroscopy

Raman spectra were recorded at room temperature, with the samples in powder form, on a LabRAM HR spectrometer (Horiba Jobin Yvon), previously calibrated and equipped with a liquid-nitrogen-cooled CCD detector. A He-Ne laser (633 nm) was used as the excitation source, with 9.0 mW at the sample, focused by a 20× long-working-distance objective. A grating of 1800 lines/mm was used, giving a spectral resolution of approximately 3 cm^{-1}. The spectra were recorded between 80 and 2000 cm^{-1}, with three acquisitions of 30 s each, and all samples were measured on the same day and under the same conditions, at a single spot per sample. In the analysis, a baseline estimated by the asymmetric least squares method (EILERS; BOELENS, 2005) ($\lambda = 10^6$, $p = 0.005$) was subtracted from each spectrum, and the spectra were normalized to the intensity of the band at about 299 cm^{-1}. The full width at half maximum (FWHM) of this band was obtained by least-squares fitting of the 250–370 cm^{-1} region with a Voigt profile whose Gaussian component was fixed at the instrumental resolution (3 cm^{-1}), together with a weak component at about 311 cm^{-1}, two components for the m-ZrO_2 lines at 333 and 348 cm^{-1} and a linear background. The FWHM uncertainty combines the standard error of the fit and the variation obtained by changing the fitting window (245–375 and 255–365 cm^{-1}); it does not include spot-to-spot variability, since a single spectrum was recorded per sample.

2.4. Scanning electron microscopy

CC BY

REMUNOM
ISSN 2178-6925

Received: 19/09/2026 - **Accepted:** 18/10/2026
Vol: 13.22
DOI: 10.66104/t71wyw54
Pages: 1-34

The morphology of the powders was analyzed by field-emission scanning electron microscopy (FEG-SEM) on an FEI Quanta 450 FEG microscope, operated in high vacuum, with an accelerating voltage of 20 kV and a working distance of approximately 12.6 mm. The images were acquired with a secondary-electron detector (ETD) at a magnification of 30,000×. The samples were analyzed without a conductive coating and were fixed with carbon tape on an FTO-coated glass support. The micrographs were processed identically for all samples, only with a linear, global brightness and contrast adjustment and a Gaussian filter (σ = 0.8 pixel, equivalent to about 7 nm) for noise reduction, without local adjustments. Particle size was determined with the ImageJ (Fiji) *software* (SCHINDELIN et al., 2012) from the original micrographs calibrated with the scale bar (about 9.0 nm per pixel). For each sample, 100 particles with fully visible contours, distributed over the whole image with the aid of an overlaid grid, were outlined manually, and the maximum Feret diameter was measured. Each unit with a continuous, individualized contour was considered a particle, including those joined to neighbors by incipient sintering necks. The distributions were fitted with a log-normal function and compared by the non-parametric Kruskal-Wallis and Mann-Whitney tests, with Holm correction for multiple comparisons (HOLM, 1979).

2.5. UV-Vis-NIR diffuse reflectance spectroscopy

Diffuse reflectance spectra were recorded on a Shimadzu UV-2600 spectrophotometer equipped with an ISR-2600Plus integrating sphere, in the 220–1200 nm range, with a spectral resolution of 1 nm. The reflectance (R) was converted into the Kubelka-Munk function, $F(R)$, which is proportional to the absorption coefficient of the material, according to Equation 1 (KUBELKA; MUNK, 1931):

$$F(R) = \frac{(1-R)^2}{2R} \quad (1)$$

The optical *gap* energy (E_g) was estimated by the Tauc method (TAUC; GRIGOROVICI; VANCU, 1966), using the relation given in Equation 2:

CC BY

REMUNOM
ISSN 2178-6925

Received: 19/09/2026 - **Accepted:** 18/10/2026
Vol: 13.22
DOI: 10.66104/t71wyw54
Pages: 1-34

$$[F(R)h\nu]^{1/n} = A(h\nu - E_g) \quad (2)$$

where *h* is Planck's constant, *v* is the frequency of the incident radiation, *A* is a proportionality constant and *n* depends on the nature of the electronic transition, taking the value 1/2 for allowed direct transitions and 2 for allowed indirect transitions. The E_g value was obtained by extrapolating the linear region of the $[F(R)h\nu]^{1/n}$ *versus* $h\nu$ curve to the abscissa, assuming an allowed direct transition (n = 1/2), as indicated by first-principles calculations for $La_2Zr_2O_7$, in which the valence-band maximum and the conduction-band minimum lie at the Γ point, a result obtained consistently with different functionals (LDA, GGA-PBE and GGA+U) (ABBAS et al., 2022; IQBAL et al., 2025; YANG et al., 2016). The linear fit was performed over a 0.30 eV interval centered on the point of maximum slope of the Tauc curve, located between 4.3 and 5.25 eV: 4.73–5.02 eV for LZO, 4.66–4.94 eV for LZO:Eu1%, 4.64–4.92 eV for LZO:Eu2% and 4.66–4.94 eV for LZO:Eu4%. Because the Eu^{3+} charge-transfer band overlaps the absorption edge in the doped samples, the E_g values obtained in this way were treated as apparent absorption onsets (MAKUŁA; PACIA; MACYK, 2018); differences in light scattering between the powders may also affect the shape of the spectra and the Tauc extrapolation.

2.6. Photoluminescence

Photoluminescence (PL) measurements were performed at room temperature. Down-shifting emission spectra were obtained under 355 nm excitation, using as the source a diode-pumped solid-state laser (DPSSL, model DPM-355), powered by a PSU-III-LED supply, with an output power of 10 mW. The emitted signal was collected and guided by an optical fiber to a UV-Vis-NIR spectrograph (Ocean Optics, HR4000), with a spectral resolution of up to 1.0 nm, operated with the SpectraSuite *software*. All samples were measured under the same excitation and collection conditions. The analysis was restricted to the 470–700 nm range: below about 465 nm, the detector saturated because of laser scattering and the intense host emission, and above 700 nm the second diffraction order of the laser line occurs (≈ 710 nm). Residual lines of the laser itself were also

CC BY

REMUNOM
ISSN 2178-6925

Received: 19/09/2026 - **Accepted:** 18/10/2026
Vol: 13.22
DOI: 10.66104/t71wyw54
Pages: 1-34

identified, at 531 nm (residual second harmonic of Nd, nominally at 532 nm) and at 1064 nm (fundamental), with identical position, width and intensity in all samples, including the undoped one, and were disregarded in the analysis. The Eu^{3+} contribution was isolated by subtracting the spectrum of undoped LZO and a local linear baseline, anchored at 569 and 671 nm, and the integrated intensities of the $^5D_0 \rightarrow {}^7F_J$ transitions were calculated over the narrow peaks, discounting the broad background with a moving-minimum filter (window of 35 points, about 9 nm, followed by a moving average of the same width; Figure 7b). The spectra were not corrected for the spectral response of the detection system. The asymmetry ratio was defined as $R = I(^5D_0 \rightarrow {}^7F_2)/I(^5D_0 \rightarrow {}^7F_1)$, integrating the 604–640 nm and 580.5–604 nm ranges, respectively (shaded in Figure 7b). To assess the sensitivity of *R* and of the integrated intensities to the background treatment, the calculation was repeated with the LZO spectrum scaled by 0.95, 1.00 and 1.05, with the baseline anchors displaced by ±3 nm and with moving-minimum windows of 25, 35 and 45 points (27 combinations); the median is reported, and the range of the combinations is given in parentheses in Table 3.

3. Results and Discussion

3.1. Crystal structure

The X-ray diffraction patterns of the samples and the corresponding Rietveld fits are shown in Figure 2. All intense reflections were indexed to the cubic pyrochlore structure (space group *Fd*$\bar{3}$*m*; ICSD 15165), which indicates that this is by far the main phase in all samples; the additional weak reflections, from m-ZrO_2 and from the FTO substrate, are discussed below. In addition to the reflections common to the pyrochlore and fluorite structures, such as (222), (400), (440) and (622), the superstructure reflections (111), (311), (331) and (511)/(333) are observed, marked with asterisks; they arise from the ordering of cations and oxygen vacancies and do not exist in the defect fluorite. The presence of these reflections confirms the formation of long-range ordered pyrochlore at 1200 °C, in agreement

CC BY

REMUNOM
ISSN 2178-6925

Received: 19/09/2026 - **Accepted:** 18/10/2026
Vol: 13.22
DOI: 10.66104/t71wyw54
Pages: 1-34

with Panghal et al. (2019), and contrasts with LZO:Eu^{3+} nanoparticles prepared by chemical routes, whose diffraction patterns do not show these reflections (ALAPARTHI et al., 2014; POKHREL; ALCOUTLABI; MAO, 2017; POKHREL et al., 2017).

Figure 2. X-ray diffraction patterns (Co Kα radiation) and Rietveld fits of the samples: a) LZO; b) LZO:Eu1%; c) LZO:Eu2%; d) LZO:Eu4%.

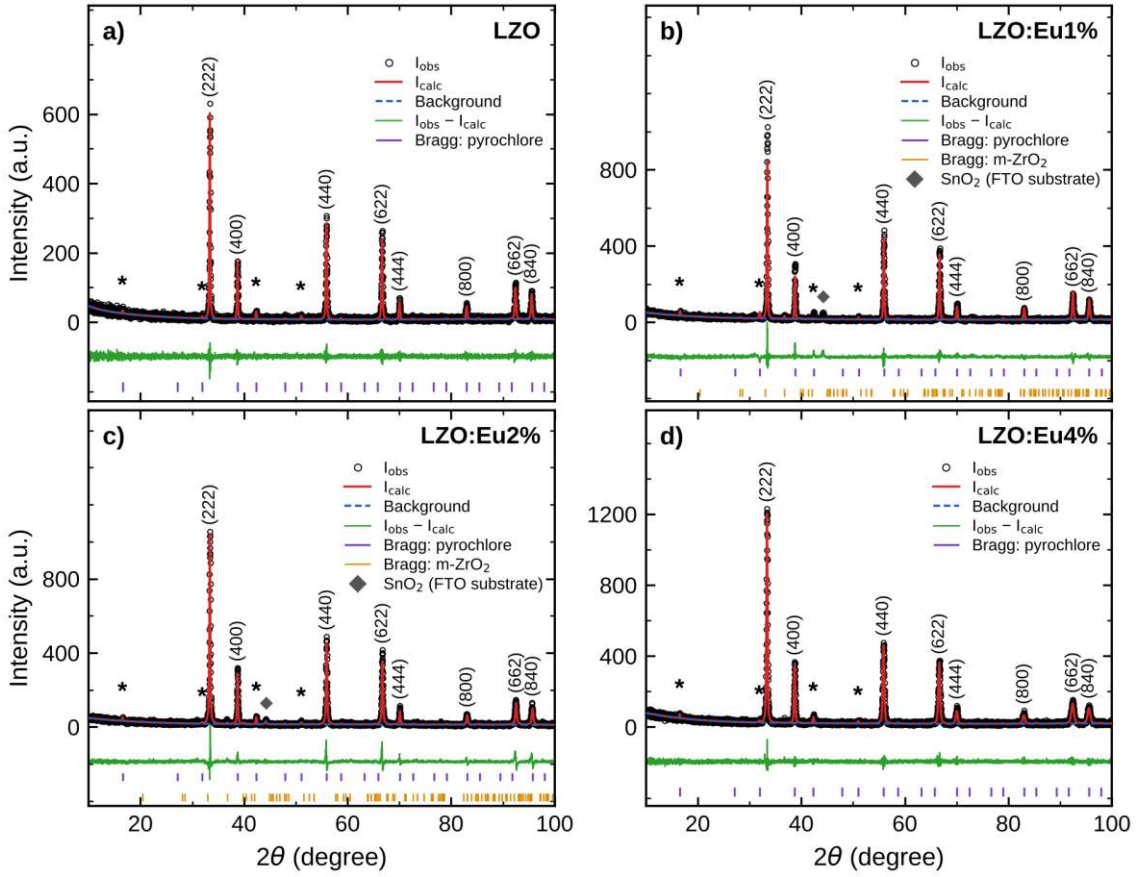

Source: Prepared by the authors (2026).

The circles represent the experimental data (I_{obs}); the red line, the calculated profile (I_{calc}); the dashed blue line, the background; the green line, the difference $I_{obs} - I_{calc}$; the purple ticks, the Bragg positions of the pyrochlore phase; and the orange ticks, those of m-ZrO_2. Miller indices identify the main reflections; asterisks (*), the superstructure reflections of the ordered pyrochlore; and the diamond, the (200) reflection of SnO_2 from the FTO substrate.

The refined parameters are summarized in Table 2. For LZO and LZO:Eu4%, the refinement was performed with the pyrochlore phase only, with no

CC BY

REMUNOM
ISSN 2178-6925

Received: 19/09/2026 - **Accepted:** 18/10/2026
Vol: 13.22
DOI: 10.66104/t71wyw54
Pages: 1-34

unindexed reflections in the difference curve. For LZO:Eu1% and LZO:Eu2%, monoclinic zirconia (m-ZrO_2) was included as a secondary phase because of weak reflections, such as (111), at about 36.7°; including La_2O_3 resulted in a negligible fraction, and this phase was disregarded. The presence of a small amount of m-ZrO_2 in all samples, including those in which it is not resolved by XRD, is confirmed by Raman spectroscopy (Section 3.2). The reflection at 44.3° observed in these two samples corresponds to the (200) plane of SnO_2 from the FTO substrate and was not included in the model. The *wR* values, between 17 and 27%, largely reflect the low counts of the data (maximum intensity between about 630 and 1,230 counts), which also raise the expected index and bring the GOF close to 1 (between 1.02 and 1.12); therefore, the GOF should not be read, on its own, as proof of the adequacy of the model. The difference curves show systematic residuals at the most intense reflections, especially for LZO:Eu1% and LZO:Eu2%, consistent with the sample displacement relative to the focal plane, discussed below. Thus, the agreement indices and lattice parameters should be regarded as indicative.

Table 2. Rietveld refinement parameters of the samples.

Sample	Phases in the model	*a* (Å)	*wR* (%)	GOF	χ^2_{red}
LZO	Pyrochlore	10.8087(3)	26.60	1.12	1.26
LZO:Eu1%	Pyrochlore + m-ZrO_2	10.8059(2)	19.64	1.02	1.04
LZO:Eu2%	Pyrochlore + m-ZrO_2	10.7914(3)	20.72	1.09	1.18
LZO:Eu4%	Pyrochlore	10.8066(3)	17.00	1.06	1.12

Source: Prepared by the authors (2026).
Note: *a*: lattice parameter, with the statistical uncertainty (esd) in the last digit given in parentheses; the systematic uncertainty associated with sample displacement is of the order of 0.01 Å; *wR*: weighted profile index; GOF: goodness of fit; χ^2_{red}: reduced chi-square.

The lattice parameters, between 10.791 and 10.809 Å, are close to the value of the crystallographic card (10.786 Å) and to that reported for LZO obtained by solid-state reaction at 1200 °C (10.802 Å; PANGHAL et al., 2019). The substitution of La^{3+} (ionic radius 1.16 Å) by Eu^{3+} (1.066 Å), both with coordination number 8 (SHANNON, 1976) and the same charge, should cause a contraction of the unit cell (ALAPARTHI et al., 2014). Based on the variation reported for $(La_{1-x}Eu_x)_2Zr_2O_7$

CC BY

REMUNOM
ISSN 2178-6925

Received: 19/09/2026 - **Accepted:** 18/10/2026
Vol: 13.22
DOI: 10.66104/t71wyw54
Pages: 1-34

ceramics, whose lattice parameter decreases from 10.80 Å (x = 0) to 10.74 Å (x = 0.5) (ZHU et al., 2018), a contraction of only 0.001 to 0.005 Å is expected for 1 to 4 mol% Eu^{3+}. Although the statistical uncertainties of the refined lattice parameters are small (0.0002–0.0003 Å; Table 2), this variation is smaller than the systematic uncertainty introduced by the sample displacement relative to the focal plane of the diffractometer, which directly affects the peak positions and is larger for LZO:Eu1% and LZO:Eu2%, measured on an FTO substrate. Because the samples were not measured on the same type of support, a direct comparison of their lattice parameters is limited. Accordingly, no trend of the lattice parameter with Eu^{3+} content can be resolved experimentally; this result indicates the absence of a resolvable variation, not a demonstration of structural invariance, and the expected contraction cannot be resolved with these data. The absence of europium-containing phases detectable by XRD and the retention of the pyrochlore structure are compatible with substitutional incorporation of Eu^{3+} on the La^{3+} site, which remains the predominant structural hypothesis and is consistent with its characteristic luminescence (Section 3.5). However, these data do not show that all Eu^{3+} occupies La^{3+} sites: the Eu^{3+} contents are nominal, and the fraction effectively incorporated into the pyrochlore phase, as well as the incorporation of part of the Eu^{3+} into secondary phases, surfaces or intergranular regions, cannot be determined with these data.

3.2. Raman spectroscopy

The Raman spectra (Figure 3a) are dominated by an intense band at 299 cm^{-1} and show bands at 394, 493 and 515 cm^{-1}, characteristic of the pyrochlore structure of $La_2Zr_2O_7$. The band at about 300 cm^{-1} comprises the A_{1g} and E_g modes, associated with vibrations of the oxygen anions in the ZrO_6 octahedron, and the bands at 396.8, 493.6 and 516.8 cm^{-1} reported for LZO are assigned to T_{2g} stretching modes of the La–O and Zr–O bonds (PANGHAL et al., 2019). The individual assignments of these modes vary in the literature (GLERUP; NIELSEN; POULSEN, 2001), but the number of observed bands is the relevant criterion to

CC BY

REMUNOM
ISSN 2178-6925

Received: 19/09/2026 - **Accepted:** 18/10/2026
Vol: 13.22
DOI: 10.66104/t71wyw54
Pages: 1-34

distinguish pyrochlore from fluorite. Whereas the defect fluorite has a single Raman-active mode (T_{2g}), the ordered pyrochlore has six (POKHREL; ALCOUTLABI; MAO, 2017); thus, the observation of several narrow bands confirms, on the local scale, the pyrochlore order indicated by the superstructure reflections in XRD.

In addition to these bands, all samples, including LZO, show weak, narrow lines at 179, 190, 224, 333, 348, 381, 476, 559, 615 and 637 cm^{-1} (triangles in Figure 3a), which correspond to the characteristic spectrum of monoclinic zirconia (m-ZrO_2) (KIM; HAMAGUCHI, 1997). These lines indicate a small fraction of residual ZrO_2, also identified by XRD in LZO:Eu1% and LZO:Eu2% (Section 3.1), to which Raman spectroscopy is particularly sensitive. The likely origin is the hydration and carbonation of La_2O_3, used without prior drying, which reduce the effective amount of lanthanum weighed and leave a small excess of ZrO_2; for this reason, Panghal et al. (2019) calcined the precursor oxides at 1100 °C before weighing. Incomplete reaction in 4 h at 1200 °C and, to a lesser extent, wear of the zirconia balls during milling may also contribute; however, the absence of lanthanum-containing phases in the refinement favors the lanthanum-deficiency hypothesis. The ratio between the intensities of the m-ZrO_2 lines and that of the 299 cm^{-1} band ranges from 0.12 to 0.22, with no trend with Eu^{3+} content; this residue therefore does not explain the trends discussed below, although the m-ZrO_2 lines at 333 and 348 cm^{-1} overlap the base of the 299 cm^{-1} band.

CC BY

REMUNOM
ISSN 2178-6925

Received: 19/09/2026 - **Accepted:** 18/10/2026
Vol: 13.22
DOI: 10.66104/t71wyw54
Pages: 1-34

Figure 3. Raman spectra of the samples (λ_{exc} = 633 nm): a) 85–860 cm^{-1} region, after baseline subtraction and normalization to the 299 cm^{-1} band; b) 1250–1950 cm^{-1} region, showing the $^5D_0 \rightarrow {}^7F_4$ emission of Eu^{3+}.

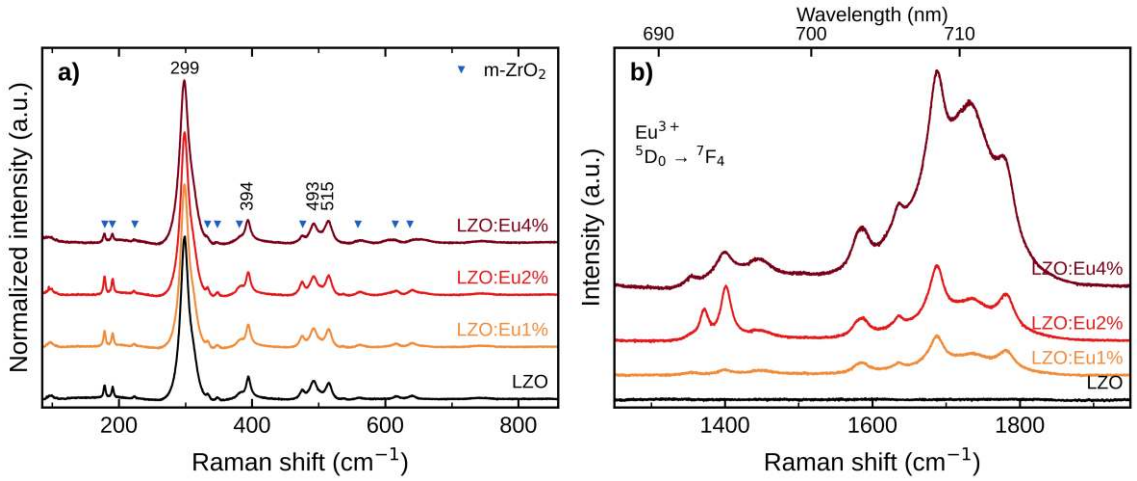

Source: Prepared by the authors (2026).

The spectra are vertically offset for clarity. In a), the numbers indicate the positions of the pyrochlore bands, and the triangles, the lines of monoclinic zirconia (m-ZrO_2); in b), the top axis indicates the wavelength corresponding to each Raman shift.

The 299 cm^{-1} band was fitted with a Voigt profile (Section 2.3). The FWHM obtained is 14.5 ± 0.2 cm^{-1} for LZO, 14.5 ± 0.2 cm^{-1} for LZO:Eu1%, 14.8 ± 0.2 cm^{-1} for LZO:Eu2% and 16.5 ± 0.2 cm^{-1} for LZO:Eu4%, and the band position varies by less than 0.7 cm^{-1}. The increase of 2.0 cm^{-1} for LZO:Eu4% relative to LZO is about ten times the estimated uncertainty and persists when the fitting window is changed, whereas the difference for LZO:Eu2% (0.3 cm^{-1}) is comparable to the uncertainty and was not interpreted. Because the fit includes the m-ZrO_2 lines at 333 and 348 cm^{-1} and the weak component at about 311 cm^{-1}, whose relative area (0.15–0.16) does not change with Eu^{3+} content, the broadening is not explained by these overlapping contributions. The instrumental contribution is the same for all samples, which were measured under identical conditions. A possible $^5D_0 \rightarrow {}^7F_3$ emission of Eu^{3+}, which under 633 nm excitation would occur between about 170 and 530 cm^{-1} (640–655 nm), is not observed as additional bands in this region and should therefore be small, although it cannot be completely ruled out. Since a single spot was measured per sample, the uncertainty does not include spatial variability.

CC BY

REMUNOM
ISSN 2178-6925

Received: 19/09/2026 - **Accepted:** 18/10/2026
Vol: 13.22
DOI: 10.66104/t71wyw54
Pages: 1-34

Because the 299 cm^{-1} band involves vibrations of the oxygen sublattice (PANGHAL et al., 2019), the increase in its width for LZO:Eu4% is compatible with increased local disorder at this content, a behavior similar to that reported for LZO:Eu^{3+} nanoparticles, in which the broadening of the band at about 302 cm^{-1} was associated with increasing localized disorder upon doping (POKHREL; ALCOUTLABI; MAO, 2017). This broadening, however, does not identify the specific defects involved.

In the doped samples, bands are also observed between about 1350 and 1800 cm^{-1} (Figure 3b), which are absent in LZO. Converted to wavelength, these bands lie between 690 and 715 nm, the region of the $^5D_0 \rightarrow {}^7F_4$ transition of Eu^{3+}, observed at about 710 nm in LZO:Eu^{3+} samples (GUPTA et al., 2019; POKHREL; ALCOUTLABI; MAO, 2017). They are therefore assigned to Eu^{3+} emission excited by the laser, not to vibrational modes. For this reason, Pokhrel, Alcoutlabi and Mao (2017) used 785 nm excitation in the Raman characterization of LZO:Eu^{3+}. Because the laser energy (1.96 eV, or 15,798 cm^{-1}) is lower than that of the $^5D_0$ level (about 17,300 cm^{-1}, according to the position of the $^5D_0 \rightarrow {}^7F_0$ transition; Section 3.5), this excitation does not occur from the ground state; possible pathways, such as phonon-assisted absorption from thermally populated ^7F_J levels or excitation via defect states, are hypotheses that were not investigated here. Because these bands are absent in LZO, they also cannot be assigned to the red emission associated with oxygen vacancies, reported at about 707 nm for undoped LZO (GUPTA et al., 2019). Here, this emission confirms the presence of optically active Eu^{3+} in the doped samples. Its intensity increases with dopant content and its profile changes, with narrower lines for LZO:Eu2% and broader bands for LZO:Eu4%, which is consistent with greater heterogeneity of the sites occupied by Eu^{3+} at the highest content.

3.3. Morphology

The micrographs (Figure 4) show, for all samples, irregular to approximately equiaxed particles gathered in agglomerates of a few micrometers. Neighboring

CC BY

REMUNOM
ISSN 2178-6925

Received: 19/09/2026 - **Accepted:** 18/10/2026
Vol: 13.22
DOI: 10.66104/t71wyw54
Pages: 1-34

particles show contacts with incipient neck formation, characteristic of the initial stage of sintering during the treatment at 1200 °C, and there is porosity between the agglomerates.

Figure 4. Scanning electron micrographs (secondary electrons, 30,000×) of the samples: a) LZO; b) LZO:Eu1%; c) LZO:Eu2%; d) LZO:Eu4%.

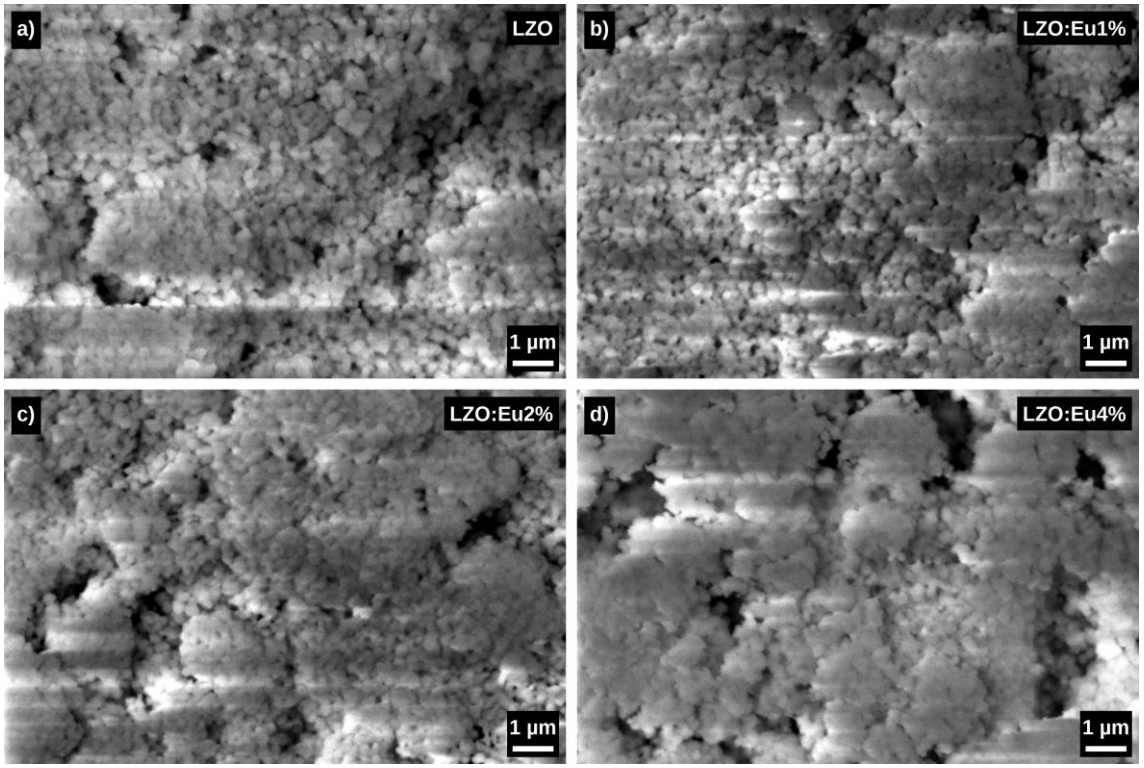

Source: Prepared by the authors (2026).

The images were subjected only to a global linear contrast adjustment and a mild Gaussian filter, as described in Section 2. The bright horizontal bands, more evident in LZO:Eu2% and LZO:Eu4%, result from electrostatic charging of the samples, which were not coated with a conductive layer, and do not correspond to microstructural features; for the same reason, the LZO:Eu4% image is less sharp.

The Feret diameter distributions, obtained by measuring 100 particles per sample, are shown in Figure 5. The mean diameters are 298 ± 44 nm for LZO, 324 ± 44 nm for LZO:Eu1%, 318 ± 43 nm for LZO:Eu2% and 320 ± 41 nm for LZO:Eu4% (mean ± standard deviation), with unimodal distributions of similar width. The Kruskal-Wallis test indicated a significant difference among the samples ($p < 0.001$); according to the Mann-Whitney test, the three doped samples differ from

CC BY

REMUNOM
ISSN 2178-6925

Received: 19/09/2026 - **Accepted:** 18/10/2026
Vol: 13.22
DOI: 10.66104/t71wyw54
Pages: 1-34

LZO ($p \leq 0.001$) but not from each other ($p > 0.4$). After Holm correction for the six comparisons, the differences between LZO and the doped samples remain significant ($p \leq 0.006$). These sizes are consistent with the grain size reported for LZO obtained by solid-state reaction at 1200 °C (0.37 μm after 24 h; PANGHAL et al., 2019), considering the shorter treatment time used here (4 h).

Figure 5. Feret diameter distributions of the particles (100 particles per sample), with log-normal fit: a) LZO; b) LZO:Eu1%; c) LZO:Eu2%; d) LZO:Eu4%.

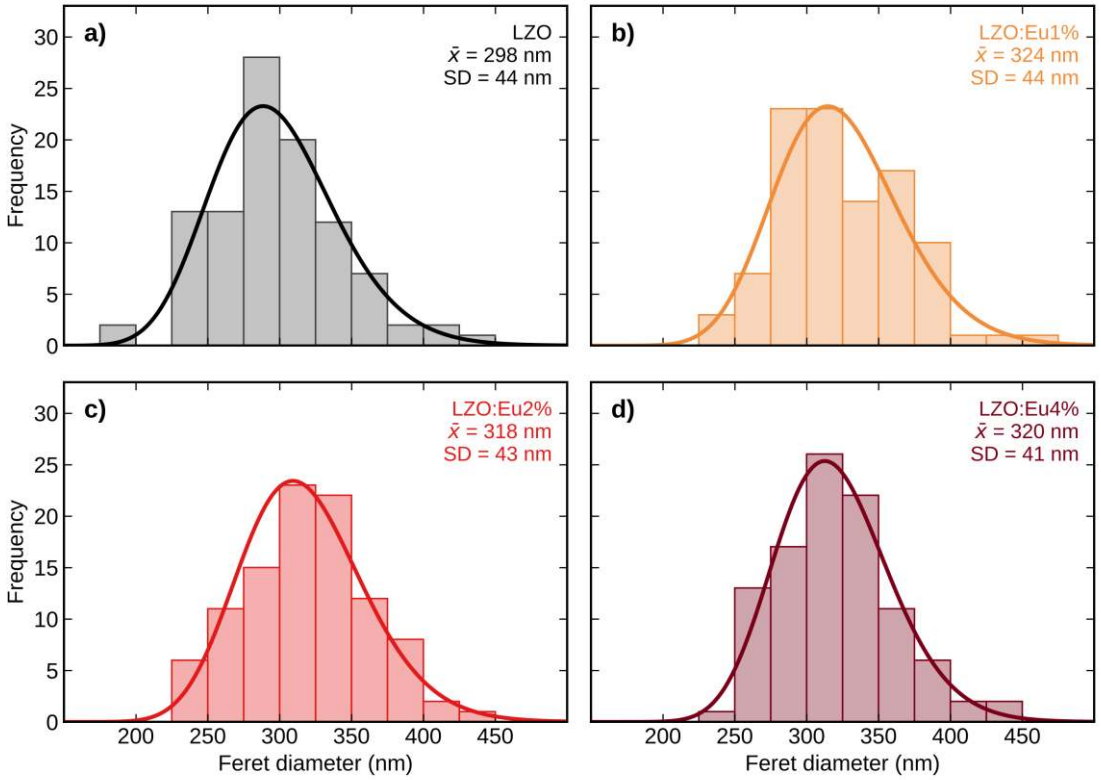

Source: Prepared by the authors (2026).

In each panel, the bars represent the frequency of particles in 25 nm bins, and the curve, the log-normal fit; the values shown correspond to the mean ($\bar{x}$) and the standard deviation (SD) of the Feret diameter.

Thus, the doped samples showed a slightly larger mean particle size, by 20 to 26 nm (7 to 9%), with no dependence on dopant content between 1 and 4 mol%. Because the 100 particles measured for each composition come from a single synthesis, the statistical tests describe differences between the particle distributions of the samples analyzed and do not demonstrate reproducibility between

CC BY

REMUNOM
ISSN 2178-6925

Received: 19/09/2026 - **Accepted:** 18/10/2026
Vol: 13.22
DOI: 10.66104/t71wyw54
Pages: 1-34

independent syntheses. For this reason, and because electrostatic charging reduces the sharpness of the contours, especially for LZO:Eu4%, this difference was not attributed to a specific effect of Eu^{3+}. The particle shape and the degree of agglomeration, in turn, do not change noticeably, which indicates that the incorporation of up to 4 mol% Eu^{3+} does not modify the morphology under the synthesis conditions used.

3.4. Optical properties: UV-Vis diffuse reflectance

The $F(R)$ spectra (Figure 6a) show negligible absorption above about 320 nm and an intense absorption edge below 300 nm, assigned to transitions from the valence band, formed mainly by O 2*p* states, to the conduction band, formed by La 5*d* and Zr 4*d* states (YANG et al., 2016). In the doped samples, the absorption between about 240 and 300 nm increases relative to LZO. The difference spectrum $\Delta F(R)$, obtained by subtracting the LZO spectrum (Figure 6b), isolates this contribution as a broad band with a maximum at 255 nm (LZO:Eu1%), 257 nm (LZO:Eu2%) and 258 nm (LZO:Eu4%), assigned to $O^{2-} \rightarrow Eu^{3+}$ charge transfer. These positions coincide with those of the charge-transfer band observed in the excitation spectra of LZO:Eu^{3+} samples (255 nm, MOHAPATRA et al., 2015; 258 nm, POKHREL; ALCOUTLABI; MAO, 2017), which confirms the assignment. The band is most intense for LZO:Eu4%, whereas the difference between the 1 and 2 mol% samples is within the uncertainty associated with the spectral subtraction. The 3 nm shift between the samples is small compared with the band width and was not interpreted. The band intensity also does not follow the Eu^{3+} content: between 1 and 4 mol%, it increases by only about 1.3 times for a fourfold content, and the negative ΔF(R) above about 300 nm indicates differences in scattering between the powders, to which the Kubelka-Munk function is sensitive. For this reason, the analysis of this band was restricted to its position.

CC BY

REMUNOM
ISSN 2178-6925

Received: 19/09/2026 - **Accepted:** 18/10/2026
Vol: 13.22
DOI: 10.66104/t71wyw54
Pages: 1-34

Figure 6. UV-Vis diffuse reflectance spectroscopy of the samples: a) Kubelka-Munk function, $F(R)$; b) difference spectrum, $\Delta F(R) = F(R)_{doped} - F(R)_{LZO}$; c) Tauc plots for an allowed direct transition.

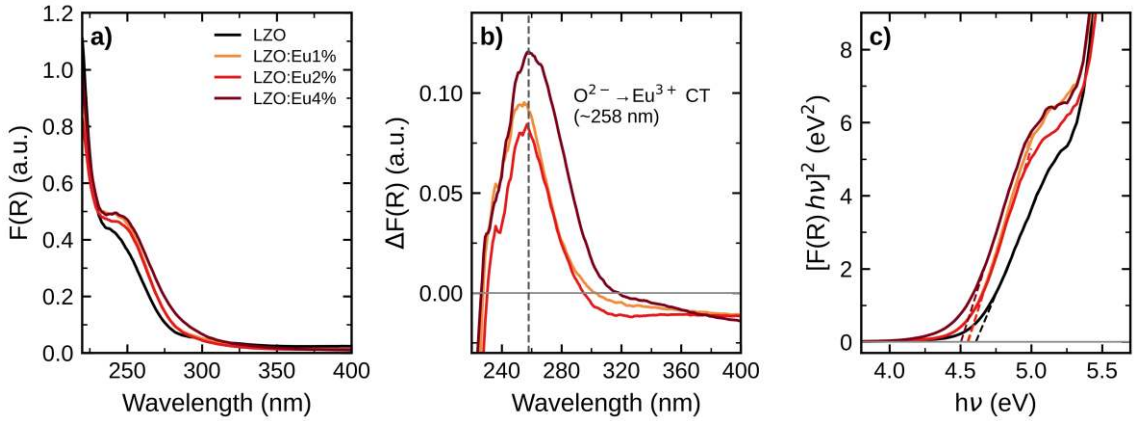

Source: Prepared by the authors (2026).

In b), the vertical dashed line indicates the maximum of the $O^{2-} \rightarrow Eu^{3+}$ charge-transfer band (about 258 nm); in c), the dashed lines represent the linear fits extrapolated to the abscissa, from which the absorption onset (E_g) is obtained.

The E_g values obtained from the Tauc plots (Figure 6c; Table 3) were 4.61 eV for LZO and 4.56, 4.55 and 4.50 eV for the samples with 1, 2 and 4 mol% Eu^{3+}, respectively; for the doped samples, these values are apparent optical onsets. The differences between the doped samples, of up to 0.06 eV, are comparable to the uncertainty associated with the choice of the linear fitting region and were not interpreted individually. The LZO value is higher than those obtained from calculations with the LDA (4.01 eV) and GGA+U (4.40 eV) functionals (ABBAS et al., 2022; YANG et al., 2016), which is consistent with the tendency of these functionals to underestimate the band gap (YANG et al., 2016). Because this underestimation is usually considerable, the fundamental band gap of LZO may lie above 4.61 eV, and this value should be understood as the optical absorption onset of the samples, which may include contributions from defect states and from the residual m-ZrO_2. The 0.11 eV reduction observed in the doped samples should not be interpreted as a narrowing of the host band gap: with contents of up to 4 mol%, the LZO band structure is unlikely to change appreciably, and the $O^{2-} \rightarrow Eu^{3+}$ charge-transfer band, centered at about 4.8 eV, overlaps the low-energy side of the absorption edge and shifts the linear extrapolation to lower energies (MAKUŁA;

CC BY

REMUNOM
ISSN 2178-6925

Received: 19/09/2026 - **Accepted:** 18/10/2026
Vol: 13.22
DOI: 10.66104/t71wyw54
Pages: 1-34

PACIA; MACYK, 2018). In addition, because the Kubelka-Munk function assumes scattering conditions that may vary between powders with different microstructures, differences in scattering between the samples, also indicated by the negative ΔF(R) above about 300 nm, may affect both the shape of the spectra and the Tauc extrapolation. Above about 5.3 eV, a second steep rise in absorption is observed, close to the limit of the measured range (220 nm, or 5.6 eV), which may correspond to the fundamental edge of the host or to higher-energy interband transitions; because it occurs near the limit of the measured range, this rise could not be analyzed.

Table 3. Optical parameters of the samples obtained by UV-Vis spectroscopy and photoluminescence.

Sample	E_g (eV)	CT band (nm)	Eu^{3+} intensity (norm.)	*R*
LZO	4.61	–	–	–
LZO:Eu1%	4.56	255	1.0 (0.9–1.1)	1.33 (1.16–1.37)
LZO:Eu2%	4.55	257	1.4 (1.2–1.5)	1.33 (1.14–1.41)
LZO:Eu4%	4.50	258	4.5 (3.8–4.9)	1.89 (1.62–2.01)

Source: Prepared by the authors (2026).
Note: E_g: optical absorption onset (Tauc, direct transition); apparent onset for the doped samples. CT band: maximum of the $O^{2-}\rightarrow Eu^{3+}$ charge-transfer band, obtained from the difference $F(R)_{doped} - F(R)_{LZO}$. Intensity: area of the $^5D_0\rightarrow{}^7F_J$ transitions (J = 0–3), normalized to the LZO:Eu1% sample. $R = I(^5D_0\rightarrow{}^7F_2)/I(^5D_0\rightarrow{}^7F_1)$. In parentheses, the range obtained by varying the background subtraction (Section 2.6); these ranges express the sensitivity to the subtraction procedure and are not statistical confidence intervals. Photoluminescence measured with λ_{exc} = 355 nm.

Table 3 summarizes the optical parameters determined by UV-Vis and photoluminescence, discussed in this section and the next.

3.5. Photoluminescence

The photoluminescence spectra under 355 nm excitation are shown in Figure 7a. LZO shows a broad emission over the whole analyzed range, with intensity decreasing toward longer wavelengths and continuing below 470 nm, a region excluded from the analysis because of detector saturation. In undoped LZO nanoparticles, emissions associated with oxygen vacancies have been reported in the violet-blue, at about 400 nm, and in the red, at about 707 nm (GUPTA et al., 2019); the emission observed here is tentatively assigned to defect states of the

CC BY

REMUNOM
ISSN 2178-6925

Received: 19/09/2026 - **Accepted:** 18/10/2026
Vol: 13.22
DOI: 10.66104/t71wyw54
Pages: 1-34

host, whose nature was not determined. The LZO spectrum also shows broad undulations at about 588 and 620 nm, which may arise from the spectral response of the detection system and which coincide with the integration windows of the $^5D_0 \rightarrow {}^7F_1$ and $^5D_0 \rightarrow {}^7F_2$ transitions. In the doped samples, the narrow lines of the $^5D_0 \rightarrow {}^7F_J$ transitions of Eu^{3+} are superimposed on this emission, and their intensity increases with dopant content.

Because the excitation energy (3.49 eV) is lower than that of the band gap and of the charge-transfer band, Eu^{3+} is excited neither through the host nor through charge transfer. Excitation may occur by direct absorption in the f–f transitions of Eu^{3+}, such as $^7F_0 \rightarrow {}^5D_4$, at about 361 nm, and by energy transfer from defect states that absorb at about 380 nm (GUPTA et al., 2019). Because the f–f lines are narrow and the 355 nm excitation is about 6 nm off resonance with $^7F_0 \rightarrow {}^5D_4$, the contribution of defect states may be predominant; this pathway favors Eu^{3+} ions close to defects, which must be taken into account when interpreting the intensity and the asymmetry ratio discussed below. Consequently, the emission spectra, and the asymmetry ratio derived from them, characterize the Eu^{3+} centers effectively excited under these conditions, which are not necessarily representative of the whole distribution of crystallographic sites occupied by the dopant. This explains the relatively low intensity of the Eu^{3+} emission compared with the host emission and limits the quantitative comparison with studies that used excitation in the charge-transfer band.

CC BY

REMUNOM
ISSN 2178-6925

Received: 19/09/2026 - **Accepted:** 18/10/2026
Vol: 13.22
DOI: 10.66104/t71wyw54
Pages: 1-34

Figure 7. Photoluminescence spectra of the samples (λ_{exc} = 355 nm): a) measured spectra; b) Eu^{3+} emission isolated by subtracting the LZO spectrum and a local baseline, with the moving-minimum background (dotted lines) and the integration windows used for *R* (shaded).

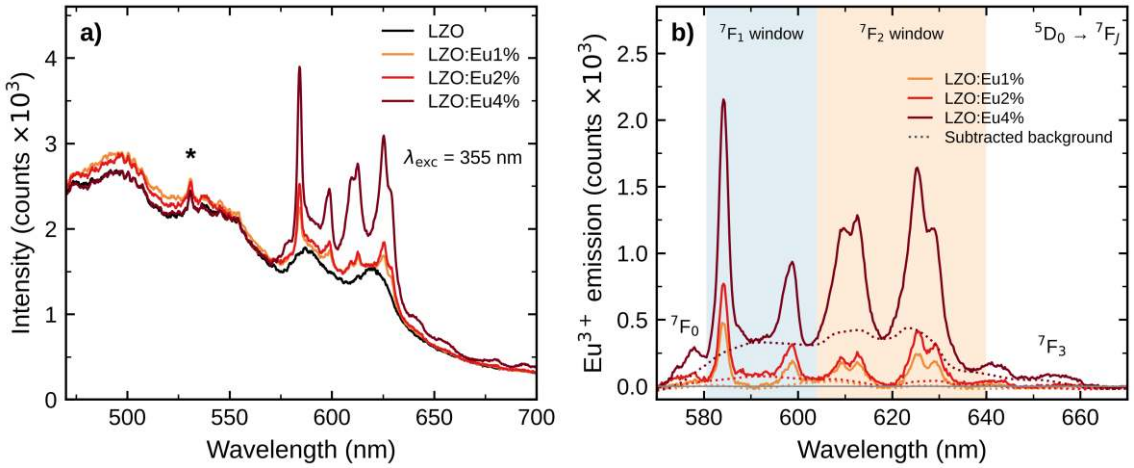

Source: Prepared by the authors (2026).

In a), the asterisk (*) indicates the residual laser line at 531 nm; in b), the $^5D_0 \rightarrow {}^7F_J$ transitions (J = 0–3) are labeled, the shaded areas correspond to the $^5D_0 \rightarrow {}^7F_1$ (580.5–604 nm) and $^5D_0 \rightarrow {}^7F_2$ (604–640 nm) integration windows, and the dotted lines show the broad background discounted before integration.

The isolated Eu^{3+} emission (Figure 7b) shows lines at about 578 nm ($^5D_0 \rightarrow {}^7F_0$), 584.2 and 598.8 nm ($^5D_0 \rightarrow {}^7F_1$), 612.6 and 625.4 nm, with shoulders at about 609 and 629 nm ($^5D_0 \rightarrow {}^7F_2$), and between 640 and 655 nm ($^5D_0 \rightarrow {}^7F_3$). These positions agree with those reported for LZO:Eu^{3+} (ALAPARTHI et al., 2014; MOHAPATRA et al., 2015). The splitting of the $^5D_0 \rightarrow {}^7F_1$ transition into two components is expected for a trigonal crystal field, such as that of the La^{3+} site in pyrochlore (D_{3d}), and has been reported for the $Gd_2Ti_2O_7$:Eu^{3+} pyrochlore (BINNEMANS, 2015). On the other hand, the observation of the $^5D_0 \rightarrow {}^7F_0$ transition, allowed only in sites of C_n, C_{nv} or C_s symmetry (BINNEMANS, 2015), and the intensity of the electric-dipole $^5D_0 \rightarrow {}^7F_2$ transition (BINNEMANS, 2015) indicate that part of the Eu^{3+} ions occupy environments without an inversion center. Possible environments include distorted sites near oxygen vacancies, antisite defects or the particle surface (POKHREL; ALCOUTLABI; MAO, 2017), but the spectral resolution and the absence of site-selective and lifetime measurements do not allow the number of emitting sites or their individual contributions to be determined. The

CC BY

REMUNOM
ISSN 2178-6925

Received: 19/09/2026 - **Accepted:** 18/10/2026
Vol: 13.22
DOI: 10.66104/t71wyw54
Pages: 1-34

$^5D_0 \rightarrow {}^7F_2$ lines are, however, narrow and constant in position in all samples, which suggests well-defined sites rather than a continuous distribution of environments. In addition to pyrochlore sites adjacent to defects, these emissions may include contributions from Eu^{3+} incorporated into the residual m-ZrO_2 or segregated at particle surfaces and boundaries, possibilities that cannot be distinguished with the available data.

The integrated intensity of the Eu^{3+} emission (Table 3) increased in the ratio 1.0 : 1.4 : 4.5 for the samples with 1, 2 and 4 mol%. The increase is not proportional to the dopant content: from 1 to 2 mol%, the intensity increases 1.4 times, less than twofold, and from 2 to 4 mol%, about 3.2 times, more than twofold. The more-than-proportional increase between 2 and 4 mol% would not be expected for a single population of ions directly excited in the f–f transitions, whose absorption increases linearly with concentration. This behavior may indicate that, in LZO:Eu4%, a larger fraction of the ions occupies sites with different absorption or emission efficiency, in agreement with the increase in *R* discussed below; however, the observed integrated emission depends on the collection geometry, the packing of the powders and the instrumental response, so that comparing absolute intensities between powders measured with fiber-optic collection is semiquantitative and does not allow the difference to be attributed to changes in intrinsic luminescence efficiency. The irregular variation between 1, 2 and 4 mol% is consistent with this limitation. No decrease in the integrated emission was observed up to 4 mol% under the experimental conditions used, which was expected, since the contents were chosen below those at which quenching was observed in nanoparticles (ALAPARTHI et al., 2014; POKHREL; ALCOUTLABI; MAO, 2017) and up to the optimum concentration reported for samples prepared by gel combustion (MOHAPATRA et al., 2015); since neither quantum yields nor lifetimes were measured, this observation does not exclude concentration-dependent non-radiative processes, and the quenching concentration in this system remains undetermined.

The asymmetry ratio was *R* = 1.33 for the samples with 1 and 2 mol% and increased to 1.89 for LZO:Eu4%. The ranges obtained by varying the background

CC BY

REMUNOM
ISSN 2178-6925

Received: 19/09/2026 - **Accepted:** 18/10/2026
Vol: 13.22
DOI: 10.66104/t71wyw54
Pages: 1-34

subtraction (Table 3) do not overlap between LZO:Eu4% and the other samples, so this increase does not result from the choice of background; nevertheless, the broad residue of the host emission, more evident for LZO:Eu4% (Figure 7b), makes the absolute values of *R* dependent on the subtraction procedure. These values lie between that expected for Eu^{3+} in the centrosymmetric site of the ordered pyrochlore ($R \approx 0.4$; HOLLIDAY et al., 2013) and those reported for LZO:Eu^{3+} nanoparticles ($R = 3.4–4.7$; GUPTA et al., 2019). This comparison is qualitative, because the reference values were obtained under other excitation and detection conditions and, in the case of Holliday et al. (2013), by time-resolved spectroscopy. Thus, the samples obtained by solid-state reaction have a more ordered local environment than the nanoparticles, in agreement with the superstructure reflections observed by X-ray diffraction, but a fraction of the Eu^{3+} ions occupies distorted sites. Three levels of interpretation should be distinguished here. The experimental result is a change in the optical environment of the excited Eu^{3+} centers at 4 mol%, shown by the increase in *R*. Its interpretation as increased local structural distortion is plausible and is supported by the broadening of the 299 cm^{-1} Raman band (Section 3.2). The specific defects responsible, however, have not been identified. Within these limits, the increase in *R* for LZO:Eu4% provides evidence compatible with a larger fraction of distorted sites at this content, a trend similar to the gradual increase in disorder with Eu^{3+} concentration reported for nanoparticles (POKHREL; ALCOUTLABI; MAO, 2017). It should be considered, however, that 355 nm excitation may favor Eu^{3+} ions close to defects, so that *R* tends to overestimate the contribution of distorted sites; selective excitation and lifetime measurements would allow the populations of each site to be quantified, as done by Holliday et al. (2013).

Some limitations should be considered in interpreting these results. Each composition corresponds to a single synthesis, and the Eu^{3+} content is nominal, without verification by elemental analysis. The 1 and 2 mol% samples were measured by XRD on an FTO substrate and the others were not, which limits the comparison of lattice parameters. Photoluminescence was excited at 355 nm, outside the charge-transfer band, without excitation spectra, lifetime measurements

CC BY

REMUNOM
ISSN 2178-6925

Received: 19/09/2026 - **Accepted:** 18/10/2026
Vol: 13.22
DOI: 10.66104/t71wyw54
Pages: 1-34

or spectral-response correction, and the conclusion about local disorder rests mainly on the 4 mol% sample. The Raman band width was obtained from a single spectrum per sample. These limitations do not change the qualitative trends discussed, but they indicate that the evolution of local disorder with Eu^{3+} content should be confirmed by studies with more compositions and time-resolved techniques.

4. Conclusion

Undoped $La_2Zr_2O_7$ and $La_2Zr_2O_7$ doped with 1, 2 and 4 mol% Eu^{3+} were obtained by solid-state reaction at 1200 °C. X-ray diffraction with Rietveld refinement showed the cubic pyrochlore structure as the main phase, with the superstructure reflections that characterize the long-range ordering of cations and oxygen vacancies, and no lattice-parameter trend resolvable within the experimental uncertainty, compatible with substitutional incorporation of Eu^{3+} on the La^{3+} site. Raman spectroscopy confirmed, on the local scale, the vibrational modes of the ordered pyrochlore and revealed a small fraction of residual monoclinic ZrO_2 in all samples, including the undoped one, most likely due to the hydration of the La_2O_3 used without prior drying, and with no trend with Eu^{3+} content. The particles, with mean Feret diameters between 298 and 324 nm and partially sintered, were slightly larger in the doped samples, with no dependence on Eu^{3+} content and no change in shape; since a single synthesis was analyzed per composition, this difference was not attributed to Eu^{3+}.

The host showed an absorption onset of 4.61 eV (Tauc, direct transition), and doping introduced the $O^{2-} \rightarrow Eu^{3+}$ charge-transfer band between 255 and 258 nm, whose overlap with the absorption edge explains the apparent reduction of this onset to as low as 4.50 eV. Under 355 nm excitation, the doped samples showed the $^5D_0 \rightarrow {}^7F_J$ emissions of Eu^{3+}, whose intensity increased with dopant content, more than proportionally between 2 and 4 mol%, and no decrease in the integrated emission was observed up to 4 mol% under the experimental conditions used. The asymmetry ratio, between 1.33 and 1.89, lay between the values expected for the

CC BY

REMUNOM
ISSN 2178-6925

Received: 19/09/2026 - **Accepted:** 18/10/2026
Vol: 13.22
DOI: 10.66104/t71wyw54
Pages: 1-34

centrosymmetric site of the ideal pyrochlore and those reported for nanoparticles, suggesting a more ordered local environment than that of nanoparticles prepared by chemical routes, but with a fraction of the Eu^{3+} ions in distorted sites. The increase in the asymmetry ratio for the 4 mol% Eu^{3+} sample, together with the broadening of the 299 cm^{-1} Raman band (FWHM from 14.5 ± 0.2 to 16.5 ± 0.2 cm^{-1}), constitutes evidence compatible with increased local disorder around the optically excited Eu^{3+} centers at this content; this interpretation remains a hypothesis supported by convergent experimental indications, and the specific defects involved were not identified, even though the long-range pyrochlore order is preserved.

These results indicate that solid-state reaction produces a $La_2Zr_2O_7$ host with a well-established pyrochlore order, in which Eu^{3+} acts as a red-emitting center and provides indications of the local disorder introduced by doping. In order of experimental robustness, the main results are: (i) the formation of ordered pyrochlore in 4 h at 1200 °C with up to 4 mol% Eu^{3+}; (ii) the characteristic Eu^{3+} emission and the determination, from the diffuse reflectance difference spectrum, of the $O^{2-} \rightarrow Eu^{3+}$ charge-transfer band in the host, not reported by this technique in the studies consulted; (iii) the asymmetry ratio values, intermediate between those of the ideal pyrochlore and those of nanoparticles, with an increase for the 4 mol% sample that does not depend on the choice of background; and (iv) the proposed interpretation of this increase as increased local disorder. As perspectives, we suggest prior drying of La_2O_3 to eliminate the residual ZrO_2; repetition of the syntheses and elemental analysis of the Eu^{3+} content; excitation in the charge-transfer band, excitation spectra and lifetime measurements, to quantify the populations of Eu^{3+} sites; extension to higher dopant contents, to determine the quenching concentration in this system; and the use of near-infrared excitation in Raman measurements, to avoid overlap with the Eu^{3+} luminescence.

CC BY

REMUNOM
ISSN 2178-6925

Received: 19/09/2026 - **Accepted:** 18/10/2026
Vol: 13.22
DOI: 10.66104/t71wyw54
Pages: 1-34

References

Abbas, Z., et al. "A First-Principles Investigation on the Structural, Optoelectronic, and Thermoelectric Properties of Pyrochlore Oxides ($La_2Tm_2O_7$ (Tm = Hf, Zr)) for Energy Applications." *International Journal of Molecular Sciences*, vol. 23, no. 23, 2022, article 15266, https://doi.org/10.3390/ijms232315266.

Alaparthi, S. B., et al. "Europium Doped Lanthanum Zirconate Nanoparticles with High Concentration Quenching." *Materials Research Bulletin*, vol. 49, 2014, pp. 114–18, https://doi.org/10.1016/j.materresbull.2013.08.057.

Binnemans, K. "Interpretation of Europium(III) Spectra." *Coordination Chemistry Reviews*, vol. 295, 2015, pp. 1–45, https://doi.org/10.1016/j.ccr.2015.02.015.

Deiseroth, H. J., and H. Müller-Buschbaum. "Ein Beitrag zur Pyrochlorstruktur an $La_2Zr_2O_7$." *Zeitschrift für anorganische und allgemeine Chemie*, vol. 375, 1970, pp. 152–56.

Eilers, P. H. C., and H. F. M. Boelens. *Baseline Correction with Asymmetric Least Squares Smoothing*. Leiden University Medical Centre, 2005. Technical report.

Glerup, M., O. F. Nielsen, and F. W. Poulsen. "The Structural Transformation from the Pyrochlore Structure, $A_2B_2O_7$, to the Fluorite Structure, AO_2, Studied by Raman Spectroscopy and Defect Chemistry Modeling." *Journal of Solid State Chemistry*, vol. 160, no. 1, 2001, pp. 25–32, https://doi.org/10.1006/jssc.2000.9142.

Gupta, S. K., et al. "Roles of Oxygen Vacancies and pH Induced Size Changes on Photo- and Radioluminescence of Undoped and Eu^{3+}-Doped $La_2Zr_2O_7$ Nanoparticles." *Journal of Luminescence*, vol. 209, 2019, pp. 302–15, https://doi.org/10.1016/j.jlumin.2019.01.059.

Holliday, K., et al. "TRLFS of Eu^{3+} and Cm^{3+} Doped $La_2Zr_2O_7$: A Comparison of Defect Fluorite to Pyrochlore Structures." *Journal of Nuclear Materials*, vol. 433, nos. 1–3, 2013, pp. 479–85, https://doi.org/10.1016/j.jnucmat.2012.10.028.

Holm, S. "A Simple Sequentially Rejective Multiple Test Procedure." *Scandinavian Journal of Statistics*, vol. 6, no. 2, 1979, pp. 65–70.

Iqbal, S., et al. "Exploring the Role of Hydrostatic Pressure Variation in Tailoring Essential Physical Properties of Thermodynamically Stable $La_2Zr_2O_7$ Pyrochlore Oxide for High-Performance Photovoltaics: A First Principles Calculations." *Computational and Theoretical Chemistry*, vol. 1248, 2025, article 115221, https://doi.org/10.1016/j.comptc.2025.115221.

CC BY

REMUNOM
ISSN 2178-6925

Received: 19/09/2026 - **Accepted:** 18/10/2026
Vol: 13.22
DOI: 10.66104/t71wyw54
Pages: 1-34

Kim, B.-K., and H. Hamaguchi. "Mode Assignments of the Raman Spectrum of Monoclinic Zirconia by Isotopic Exchange Technique." *Physica Status Solidi (b)*, vol. 203, no. 2, 1997, pp. 557–63.

Kubelka, P., and F. Munk. "Ein Beitrag zur Optik der Farbanstriche." *Zeitschrift für technische Physik*, vol. 12, 1931, pp. 593–601.

Kudoh, Y., H. Takeda, and H. Arashi. "In Situ Determination of Crystal Structure for High Pressure Phase of ZrO_2 Using a Diamond Anvil and Single Crystal X-Ray Diffraction Method." *Physics and Chemistry of Minerals*, vol. 13, 1986, pp. 233–37, https://doi.org/10.1007/BF00308274.

Makuła, P., M. Pacia, and W. Macyk. "How To Correctly Determine the Band Gap Energy of Modified Semiconductor Photocatalysts Based on UV–Vis Spectra." *The Journal of Physical Chemistry Letters*, vol. 9, no. 23, 2018, pp. 6814–17, https://doi.org/10.1021/acs.jpclett.8b02892.

Mohapatra, M., et al. "Photoluminescence Properties of 'Red' Emitting $La_2Zr_2O_7$:Eu Pyrochlore Ceramics for Potential Phosphor Application." *Journal of Luminescence*, vol. 166, 2015, pp. 1–7, https://doi.org/10.1016/j.jlumin.2015.04.034.

Panghal, A., et al. "Investigations of Atomic Disorder and Grain Growth Kinetics in Polycrystalline $La_2Zr_2O_7$." *Applied Physics A*, vol. 125, 2019, article 428, https://doi.org/10.1007/s00339-019-2720-8.

Pokhrel, M., M. Alcoutlabi, and Y. Mao. "Optical and X-Ray Induced Luminescence from Eu^{3+} Doped $La_2Zr_2O_7$ Nanoparticles." *Journal of Alloys and Compounds*, vol. 693, 2017, pp. 719–29, https://doi.org/10.1016/j.jallcom.2016.09.218.

Pokhrel, M., et al. "Enhance the Photoluminescence and Radioluminescence of $La_2Zr_2O_7$:Eu^{3+} Core Nanoparticles by Coating with a Thin Y_2O_3 Shell." *Optical Materials*, vol. 68, 2017, pp. 35–41, https://doi.org/10.1016/j.optmat.2016.11.008.

Rietveld, H. M. "A Profile Refinement Method for Nuclear and Magnetic Structures." *Journal of Applied Crystallography*, vol. 2, no. 2, 1969, pp. 65–71, https://doi.org/10.1107/S0021889869006558.

Schindelin, J., et al. "Fiji: An Open-Source Platform for Biological-Image Analysis." *Nature Methods*, vol. 9, no. 7, 2012, pp. 676–82, https://doi.org/10.1038/nmeth.2019.

Shannon, R. D. "Revised Effective Ionic Radii and Systematic Studies of Interatomic Distances in Halides and Chalcogenides." *Acta Crystallographica Section A*, vol. 32, no. 5, 1976, pp. 751–67, https://doi.org/10.1107/S0567739476001551.

CC BY

REMUNOM
ISSN 2178-6925

Received: 19/09/2026 - **Accepted:** 18/10/2026
Vol: 13.22
DOI: 10.66104/t71wyw54
Pages: 1-34

Subramanian, M. A., G. Aravamudan, and G. V. Subba Rao. "Oxide Pyrochlores — A Review." *Progress in Solid State Chemistry*, vol. 15, no. 2, 1983, pp. 55–143, https://doi.org/10.1016/0079-6786(83)90001-8.

Tauc, J., R. Grigorovici, and A. Vancu. "Optical Properties and Electronic Structure of Amorphous Germanium." *Physica Status Solidi (b)*, vol. 15, no. 2, 1966, pp. 627–37, https://doi.org/10.1002/pssb.19660150224.

Toby, B. H., and R. B. Von Dreele. "GSAS-II: The Genesis of a Modern Open-Source All Purpose Crystallography Software Package." *Journal of Applied Crystallography*, vol. 46, no. 2, 2013, pp. 544–49, https://doi.org/10.1107/S0021889813003531.

Yang, J., et al. "Physical Properties of $La_2B_2O_7$ (B = Zr, Sn, Hf and Ge) Pyrochlore: First-Principles Calculations." *Journal of Alloys and Compounds*, vol. 663, 2016, pp. 834–41, https://doi.org/10.1016/j.jallcom.2015.12.189.

Zhu, R., et al. "X-Ray Diffractional, Spectroscopic and Thermo-Physical Properties Analyses on Eu-Doped Lanthanum Zirconate Ceramic for Thermal Barrier Coatings." *Journal of Alloys and Compounds*, vol. 746, 2018, pp. 62–67, https://doi.org/10.1016/j.jallcom.2018.02.143.

CC BY